

# Non-diffractive computational ghost imaging

D. B. Phillips,<sup>1,3,\*</sup> Ruiqing He,<sup>1,2,3</sup> Qian Chen,<sup>2</sup> G. M. Gibson,<sup>1</sup> and M. J. Padgett<sup>1</sup>

<sup>1</sup>*School of Physics and Astronomy, Glasgow University, Glasgow. G12 8QQ. Scotland. U.K.*

<sup>2</sup>*Department of Optical Engineering, School of Electronic and Optical Engineering, Nanjing University of Science and Technology, Nanjing 210094, China*

<sup>3</sup>*These authors contributed equally to this work.*

[\\*david.phillips@glasgow.ac.uk](mailto:david.phillips@glasgow.ac.uk)

**Abstract:** Computational ghost imaging (CGI) enables an image to be recorded using a single-pixel detector. The image can be reconstructed from correlations between the scene and a series of known projected intensity patterns. In this work we investigate the performance of CGI using pseudo non-diffracting (ND) speckle patterns. We demonstrate an extended depth-of-field that is  $\sim 2$ - $3$  times greater than that achievable with conventional speckle, when only computing each intensity pattern to a single depth. In addition, the average speckle grain size of ND speckle is reduced by a factor of  $\sim 1.5$  relative to conventional speckle, which enhances the lateral Rayleigh-limit resolving power of our reconstructed images. However, the point-spread function (PSF) of our imaging system takes the form of a Bessel beam, which manifests itself as long-range correlations between speckle grains in the projected patterns. We discuss the trade-off between enhancement of the depth-of-field and the lateral resolution when using ND speckle, at the expense of a reduction in image contrast. Our work demonstrates that the tailoring of lateral and axial correlations in projected intensity patterns permits PSF engineering in CGI.

Published by The Optical Society under the terms of the [Creative Commons Attribution 4.0 License](#). Further distribution of this work must maintain attribution to the author(s) and the published article's title, journal citation, and DOI.

**OCIS codes:** (110.1758) Computational imaging; (070.3185) Invariant optical fields; (110.0180) Microscopy.

---

## References and links

1. T. Pittman, Y. Shih, D. Strekalov, and A. Sergienko, "Optical imaging by means of two-photon quantum entanglement," *Phys. Rev. A* **52**, R3429 (1995).
2. A. F. Abouraddy, B. E. Saleh, A. V. Sergienko, and M. C. Teich, "Role of entanglement in two-photon imaging," *Phys. Rev. Lett.* **87**, 123602 (2001).
3. R. S. Bennink, S. J. Bentley, and R. W. Boyd, "Two-photon coincidence imaging with a classical source," *Phys. Rev. Lett.* **89**, 113601 (2002).
4. R. S. Bennink, S. J. Bentley, R. W. Boyd, and J. C. Howell, "Quantum and classical coincidence imaging," *Phys. Rev. Lett.* **92**, 033601 (2004).
5. A. Gatti, E. Brambilla, M. Bache, and L. A. Lugiato, "Correlated imaging, quantum and classical," *Phys. Rev. A* **70**, 013802 (2004).
6. J. H. Shapiro and R. W. Boyd, "The physics of ghost imaging," *Quantum Inf. Process.* **11**, 949–993 (2012).
7. F. Ferri, D. Magatti, A. Gatti, M. Bache, E. Brambilla, and L. A. Lugiato, "High-resolution ghost image and ghost diffraction experiments with thermal light," *Phys. Rev. Lett.* **94**, 183602 (2005).
8. A. Valencia, G. Scarcelli, M. D'Angelo, and Y. Shih, "Two-photon imaging with thermal light," *Phys. Rev. Lett.* **94**, 063601 (2005).

9. D. Zhang, Y.-H. Zhai, L.-A. Wu, and X.-H. Chen, "Correlated two-photon imaging with true thermal light," *Opt. Lett.* **30**, 2354–2356 (2005).
10. J. H. Shapiro, "Computational ghost imaging," *Phys. Rev. A* **78**, 061802 (2008).
11. B. I. Erkmen and J. H. Shapiro, "Ghost imaging: from quantum to classical to computational," *Adv. Opt. Photonics* **2**, 405–450 (2010).
12. M. Levoy, "Light fields and computational imaging," *Computer* pp. 46–55 (2006).
13. B. Sun, M. P. Edgar, R. Bowman, L. E. Vittert, S. Welsh, A. Bowman, and M. Padgett, "3d computational imaging with single-pixel detectors," *Science* **340**, 844–847 (2013).
14. D. Takhar, J. N. Laska, M. B. Wakin, M. F. Duarte, D. Baron, S. Sarvotham, K. F. Kelly, and R. G. Baraniuk, "A new compressive imaging camera architecture using optical-domain compression," in "Electronic Imaging 2006," (International Society for Optics and Photonics, 2006), pp. 606509.
15. M. P. Edgar, G. M. Gibson, R. W. Bowman, B. Sun, N. Radwell, K. J. Mitchell, S. S. Welsh, and M. J. Padgett, "Simultaneous real-time visible and infrared video with single-pixel detectors," *Sci. Rep.* **5**, 10669 (2015).
16. M.-J. Sun, M. P. Edgar, D. B. Phillips, G. M. Gibson, and M. J. Padgett, "Improving the signal-to-noise ratio of single-pixel imaging using digital microscanning," *Opt. Express* **24**(10), 10476–10485 (2016).
17. Y. Bromberg, O. Katz, and Y. Silberberg, "Ghost imaging with a single detector," *Phys. Rev. A* **79**, 053840 (2009).
18. J. W. Goodman, *Introduction to Fourier Optics* (Roberts and Company Publishers, 2005).
19. J. W. Goodman, *Speckle Phenomena in Optics: Theory and Applications* (Roberts and Company Publishers, 2007).
20. D. M. Cottrell, J. M. Craven, and J. A. Davis, "Nondiffracting random intensity patterns," *Opt. Lett.* **32**, 298–300 (2007).
21. R. N. Mahalati, R. Y. Gu, and J. M. Kahn, "Resolution limits for imaging through multi-mode fiber," *Opt. Express* **21**, 1656–1668 (2013).
22. R. Y. Gu, R. N. Mahalati, and J. M. Kahn, "Noise-reduction algorithms for optimization-based imaging through multi-mode fiber," *Opt. Express* **22**, 15118–15132 (2014).
23. J. Durnin, "Exact solutions for nondiffracting beams. i. the scalar theory," *J. Opt. Soc. Am. A* **4**, 651–654 (1987).
24. J. Durnin, J. Miceli Jr, and J. Eberly, "Diffraction-free beams," *Phys. Rev. Lett.* **58**, 1499 (1987).
25. D. McGloin and K. Dholakia, "Bessel beams: diffraction in a new light," *Contemp. Phys.* **46**, 15–28 (2005).
26. T. A. Planchon, L. Gao, D. E. Milkie, M. W. Davidson, J. A. Galbraith, C. G. Galbraith, and E. Betzig, "Rapid three-dimensional isotropic imaging of living cells using bessel beam plane illumination," *Nat. Methods* **8**, 417–423 (2011).
27. Z. Bouchal, "Controlled spatial shaping of nondiffracting patterns and arrays," *Opt. Lett.* **27**, 1376–1378 (2002).
28. J. Courtial, G. Whyte, Z. Bouchal, and J. Wagner, "Iterative algorithms for holographic shaping of non-diffracting and self-imaging light beams," *Opt. Express* **14**, 2108–2116 (2006).
29. M. Boguslawski, S. Brake, J. Armijo, F. Diebel, P. Rose, and C. Denz, "Analysis of transverse anderson localization in refractive index structures with customized random potential," *Opt. Express* **21**, 31713–31724 (2013).
30. C. Paterson and R. Smith, "Higher-order bessel waves produced by axicon-type computer-generated holograms," *Opt. Commun.* **124**, 121–130 (1996).
31. T. Čížmár and K. Dholakia, "Tunable bessel light modes: engineering the axial propagation," *Opt. Express* **17**, 15558–15570 (2009).
32. F. O. Fahrbach, P. Simon, and A. Rohrbach, "Microscopy with self-reconstructing beams," *Nat. Photonics* **4**, 780–785 (2010).
33. R. E. Meyers, K. S. Deacon, A. D. Tunick, and Y. Shih, "Virtual ghost imaging through turbulence and obscurants using bessel beam illumination," *Appl. Phys. Lett.* **100**, 061126 (2012).
34. Z. Bouchal, J. Wagner, and M. Chlup, "Self-reconstruction of a distorted nondiffracting beam," *Opt. Commun.* **151**, 207–211 (1998).
35. N. D. Hardy and J. H. Shapiro, "Computational ghost imaging versus imaging laser radar for three-dimensional imaging," *Phys. Rev. A* **87**, 023820 (2013).
36. E. T. Rogers and N. I. Zheludev, "Optical super-oscillations: sub-wavelength light focusing and super-resolution imaging," *J. Opt.* **15**, 094008 (2013).
37. M. R. Dennis, A. C. Hamilton, and J. Courtial, "Superoscillation in speckle patterns," *Opt. Lett.* **33**, 2976–2978 (2008).
38. M. Berry, "A note on superoscillations associated with bessel beams," *J. Opt.* **15**, 044006 (2013).
39. Y. Bromberg and H. Cao, "Generating non-rayleigh speckles with tailored intensity statistics," *Phys. Rev. Lett.* **112**, 213904 (2014).

---

## 1. Introduction

Conventional cameras collect light that has been scattered or transmitted by an object and form an image on a multi-pixel detector array. Ghost imaging (GI) is an alternative technique that

originally emerged from experiments exploiting the quantum nature of light to record an image of an object [1]. Although initially thought to rely on quantum entanglement, it was later shown that the key property enabling GI was the spatial correlation between photons, which can also be engineered using classical light [2–6].

In the first classical GI demonstrations [7–9], a beam-splitter was used to create two copies of a beam imprinted with the same optical speckle pattern. One of these beams illuminated the object, while the other beam, which itself had never interacted with the object, was directed to a camera which measured the intensity distribution of the speckle pattern. The total intensity of the light backscattered by the object (or transmitted, in the case of a transmissive object) was also recorded using a single-pixel detector, possessing no spatial-resolution. In this configuration, the single-pixel detector measures the correlation between the projected intensity pattern and the object: a higher correlation leading to a greater intensity of light transmitted to the single-pixel detector. This process was then repeated using a large number ( $\sim 10^4$ ) of different optical speckle patterns. The information recorded by either the single-pixel detector, or the camera alone is not enough to form an image of the object. However, an image of the object can be reconstructed by performing a weighted sum of the ensemble of projected intensity patterns, each weighted by its degree of correlation with the object, which has been measured by the single-pixel detector.

More recently, computational ghost imaging (CGI) was developed, which is a classical technique that removes the need for a camera entirely [10, 11]. CGI relies on the use of spatial light modulators (SLMs) to create a series of programmed intensity patterns which are projected onto an object. A single-pixel detector is again used to measure the correlation between each pattern and the object. Using the CGI scheme, each projected intensity pattern can be calculated from the configuration of the SLM used to create it, which renders the camera arm redundant. The image is reconstructed in the same way as described above. CGI is a branch of the field now more generally known as ‘computational imaging’ [12, 13]. A related field is that of single-pixel cameras which also use spatial correlations to record images, and operate by sequentially filtering an image of a scene with a series of masking patterns, rather than projecting patterns onto the scene [14–16]. Recently single-pixel imaging techniques have attracted much interest, although we note that they suffer from poor signal-to-noise ratio in comparison with conventional detector arrays, and so are generally only competitive in spectral regions where detector arrays are unavailable.

CGI was first demonstrated by illuminating an object with a series of optical speckle patterns which were generated using a phase-only SLM [17]. The transverse intensity profile of each speckle pattern at the object plane was calculated from the known SLM configuration using the Fresnel diffraction integral [18]. Such a system can be computationally refocused (during data collection or in post-processing) to form an image of any axial plane, and so has a theoretically infinite *computational* depth-of-field (DoF). However, because the transverse intensity profile of conventional optical speckle changes upon propagation, it is necessary to know the axial position at which the object is located before an image can be unambiguously recovered. In CGI, the *local* depth-of-field, about a focal depth at which the transverse intensity profile of the projected patterns has been calculated, is determined by the axial correlation length of the speckle patterns [19]. Similarly, the lateral resolution is determined by the lateral correlation length of the speckle patterns.

In this work we investigate the use of pseudo non-diffracting (ND) speckle patterns [20] to increase the local DoF of a CGI system. The use of ND speckle removes the need to computationally refocus by recalculation of projected intensity patterns, which typically number in their thousands: the same order as the number of pixels in the reconstructed images. Such a scheme may find use when imaging objects at an unknown distance from the projector. In particular,

real-time applications of CGI may benefit, where the time taken to re-calculate the intensity of all of the projected patterns at a range of depths could be prohibitively long. For the same sized limiting aperture, ND speckle also exhibits a smaller average grain size than conventional speckle, which consequently also increases the lateral Rayleigh-limit resolving power of our imaging system. However, using ND speckle also causes a reduction in image contrast. We discuss the trade-off between enhancement in both DoF and resolving power at the expense of a concomitant reduction in image contrast, and describe how this trade-off can be controlled by tailoring the extent of lateral and axial correlations in the projected speckle patterns.

## 2. Methods

A schematic of our CGI system is shown in Fig. 1(a). A series of  $N$  speckle fields are generated using a phase-only SLM. The speckle fields propagate to a transmissive binary object, and the correlation ( $S_i$ ) between the object and the 2D transverse intensity profile ( $P_i$ ) of speckle pattern  $i$  is recorded using a photodiode; *i.e.*  $S_i$  is a measure of the total intensity transmitted through the object. An image of the object ( $I$ ) is then reconstructed using

$$I = \langle SP \rangle - \langle S \rangle \cdot \langle P \rangle, \quad (1)$$

where for example  $\langle S \rangle = \frac{1}{N} \sum_{i=1}^N S_i$  denotes an ensemble average of  $S$  over  $N$  measurements. Figure 1(b-e) shows the reconstruction of an experimentally recorded computational image using Eq. (1) with progressively increasing numbers of non-diffractive speckle patterns ( $N$ ). We also note that there are also alternative reconstruction methods using the same input data, such as linear optimisation based approaches [21]. Such methods have the potential to recover a more faithful image for a given finite number of pattern projections, but they are more computationally expensive, and can be highly susceptible to measurement noise [22].

Figure 2 shows how the SLM can be used to generate either what we term here as ‘conventional’ speckle patterns (Fig. 2(a-d)), or pseudo non-diffractive speckle patterns (Fig. 2(e-h)). In both cases the SLM is illuminated with a collimated Gaussian beam, expanded to overfill the displayed patterns. To create conventional speckle, the phase pattern displayed on the SLM is divided into super-pixels arranged within a disk of radius  $r_{max}$  (Fig. 2(a)). The SLM is placed at the back focal plane of a Fourier transforming lens (L1), and random variation of the phase of each super-pixel produces a random conventional speckle pattern at the front focal plane of L1 (Fig. 2(b)). The phase pattern shown in Fig. 2(a) is added to a phase grating (not shown), which is of higher spatial frequency than the super-pixel pattern itself. The presence of the phase grating on the SLM laterally translates the speckle pattern into the first order of the far-field diffraction pattern, away from any zero-order undiffracted light. As the size of the super-pixels is reduced, the number of speckle grains and lateral size of the resulting speckle pattern is increased (without changing the average speckle grain size), which sets the field-of-view (FoV) of the system. Therefore the size of the super-pixels can be chosen to set a reasonable FoV whilst also ensuring that the speckle pattern is well separated from other diffraction orders. Unwanted orders are then blocked using an aperture centred on the speckle pattern as shown in Fig. 1(a).

The transverse intensity profile of the conventional speckle pattern is unstable upon propagation, as demonstrated by comparing Fig. 2(b) and 2(c), and by the transverse map of field propagation shown in Fig. 2(d). This propagation instability limits the local DoF around a particular axial plane. To understand why the conventional speckle is unstable on propagation, it is helpful to consider a propagating field in terms of a superposition of plane-waves in the scalar paraxial approximation [18]. As the field propagates, the phase of each plane-wave component changes by  $k_z \cdot z$  (where  $z$  is the axial propagation distance, and  $k_z$  is the z-component of the wavenumber of each plane-wave). In our case, conventional speckle consists of a superposition of plane-wave components with a range of different values of  $k_z$  (*i.e.* light is emitted from any-

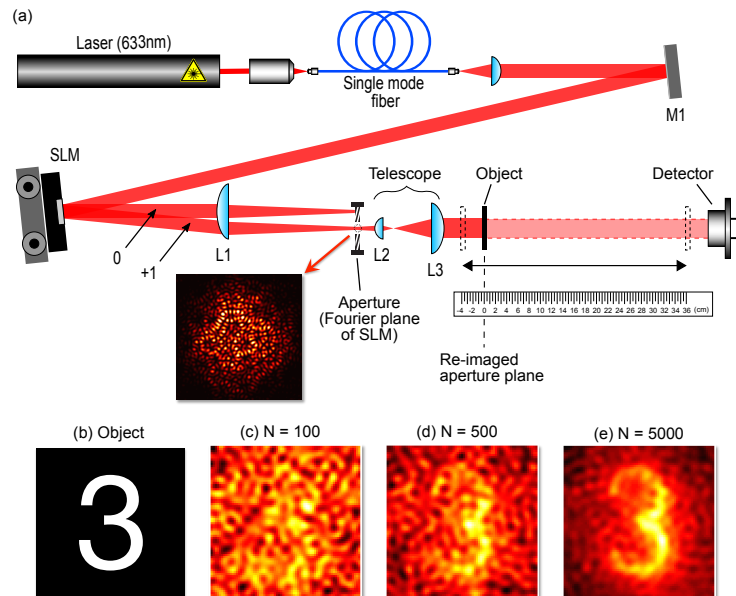


Fig. 1. (a) A schematic of our CGI setup. A 633 nm wavelength laser beam is transmitted through a single mode fibre to create a TEM<sub>00</sub> Gaussian mode. This is reflected by mirror M1 and illuminates a phase-only SLM (optically addressed Hamamatsu X8267-14) which is used to spatially modulate the phase of the beam. The beam waist of the illuminating beam is 4 mm. The SLM is placed at the back focal plane of a lens L1 of focal length 400 mm. The SLM phase modulation (which is described in Fig. 2(a,e)) generates a speckle pattern (shown in the inset) at the front focal plane of lens L1, in the +1 order of the diffracted beam. An aperture is used to select only the +1 diffraction order beam and block all other orders. A telescope (L2 and L3, of focal lengths 30 mm and 60 mm respectively) is used to magnify (by a factor of 2) and re-image the speckle pattern to the front focal plane of L3, conjugate to the front focal plane of L1. The front focal plane of L3 represents an axial position of  $z=0$ . A binary transmissive object is placed at any plane in-between L3 and a photodetector (ThorLabs PDA100A-EC) positioned at a distance of 400 mm behind L3. The photodiode records the total intensity of light transmitted through the object. (b-e) The formation of a computational ghost image using ND speckle: (b) shows a transmissive object (height 1 mm), and (c-e) show reconstructions after the projection of increasing numbers of speckle patterns.

where within the disk on the SLM). Each of these components undergoes a different relative phase change upon propagation, and so they interfere to produce different transverse intensity profiles at axially displaced planes.

In 1987 Durnin *et al.* demonstrated the generation of non-diffractive beams that have transverse intensity profiles that are invariant upon propagation [23, 24]. This was achieved by ensuring that all of the  $k_z$  components in a plane-wave decomposition of the field take the same value, so that each component undergoes an identical phase change upon propagation. Such a situation can be engineered by restricting the field in the Fourier plane of the required beam to an annular ring. This concept led to the creation of the now well-known Bessel beam that has found applications in a wide range of fields including imaging, optical micro-manipulation and optical communications [24–26]. It was subsequently shown that it was also possible to

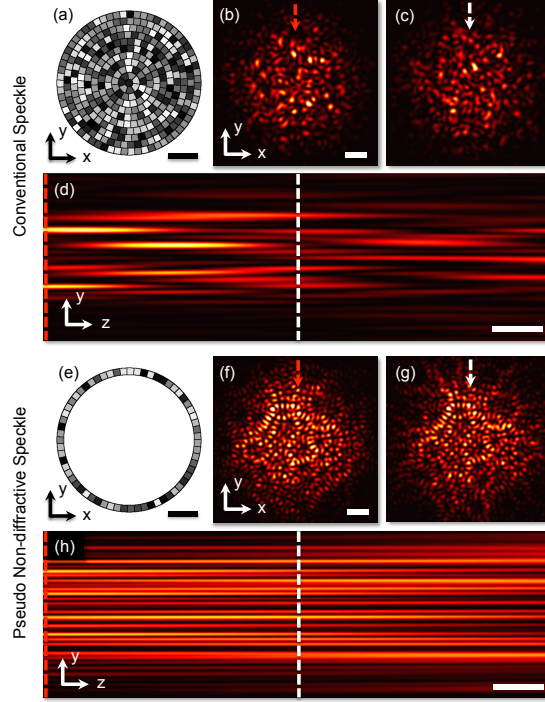


Fig. 2. Numerical simulations of speckle generation using an SLM. (a-d) Conventional speckle. (e-h) Pseudo-non-diffracting speckle. (a,e) Relative phase of super-pixels on the SLM (greyscale value maps to phase, white = 0 rad. and black =  $2\pi$  rad.). (b,f) Intensity pattern in Fourier plane of SLM. (c,g) Intensity pattern of speckle after propagation for 0.2 m. (d,h) Side-view cross-section of speckle intensity distribution over a propagation distance of 0.4 m. Red dashed lines in (d,h) correspond to planes (b,f) respectively. White dashed lines in (d,h) correspond to planes (c,g) respectively. Arrows in (b,c,f,g) indicate the vertical plane cross-section viewed in (d,h).

shape the transverse intensity profile of non-diffracting beams to produce propagation invariant speckle and a range of other non-diffractive intensity patterns [20, 27–29]. These beams are formed by modulating the amplitude and/or phase of the field around the annulus. Therefore we generate ND speckle in our experiment by displaying an arrangement of super-pixels with randomly chosen phases in an annular ring on the SLM, as shown in Fig. 2(e).

To attain an infinitely long non-diffracting length, the annulus should be infinitely thin (and perfectly imaged with a lens of infinite diameter). Of course this is not achievable in reality, and so constraining the phase on the SLM to a ring of finite width results in a speckle pattern which is non-diffracting over an extended but finite axial range, as demonstrated in Figs. 2(f-h). A pseudo ND beam such as this contains wave-vectors with a small range of  $k_z$  components. The finite stable axial range of such a beam can be estimated by considering the relative phase change of the highest and lowest  $k_z$  components as the beam propagates axially. The distance over which these two components go out of phase by  $\pi$  radians ( $z_{stable}$ ) provides a useful guide to the beam's stability:

$$z_{stable} = \frac{2\pi f^2}{k(r_{max}^2 - r_{min}^2)}, \quad (2)$$

where  $f$  is the focal length of the Fourier transforming lens,  $k$  is the wavenumber, and  $r_{max}$  and  $r_{min}$  are the outer and inner radius of the annulus in the back focal plane of the lens. Here we have expressed  $z_{stable}$  in terms of parameters in our optical set up, by considering that  $k^2 = k_r^2 + k_z^2$ , and  $k_z/k_r = f/r$ , where  $k_r$  is the lateral component of the wavenumber of each plane-wave, and  $r$  is the radial position in the back focal plane of the lens. When  $r_{min} \rightarrow 0$  (as in the case of the circular aperture used for conventional speckle generation), the stable range  $z_{stable} \rightarrow 4\pi z_R$ , where  $z_R$  is the Rayleigh range. In our experiments the thickness of the annulus was chosen so that the stable range of the ND speckle was increased by a factor of  $\sim 4$  compared to that of conventional speckle, corresponding to  $r_{min} = 0.87 r_{max}$ .

ND speckle also inherits another characteristic from the physically realisable Bessel beam: a finite axial range ( $z_{range}$ ) after which a circular ‘shadow zone’ forms, extinguishing on-axis light. This phenomenon was also described by Durnin *et al.* in [24]. Therefore:

$$z_{range} = \frac{Df}{2r_{min}}, \quad (3)$$

where  $D$  is the diameter of the Fourier transforming lens. Equation (3) shows that as  $r_{min} \rightarrow 0$ ,  $z_{range} \rightarrow \infty$  as we would expect. The shadow zone can be understood to develop at a depth where all of the rays have crossed the optical axis, and is therefore due to the finite diameter  $D$  of the Fourier transforming lens. Therefore, in contrast to the theoretically infinite computational DoF offered by conventional speckle (even with finite  $D$ ), the appearance of the shadow zone with ND speckle limits the computational DoF to a distance  $z_{range}$  beyond the Fourier transforming lens. However, as the SNR of projection CGI systems falls in proportion to the square of the object’s distance, using CGI for long distance imaging is challenging and often not practical. In addition to an increase in local DoF, ND speckle does offer a potentially advantageous alternative trade-off between image resolution, computational DoF, and contrast, which we discuss below.

### 3. Results

#### 3.1. Local depth-of-field

In Fig. 3 we demonstrate the use of ND speckle patterns to increase the local DoF around a particular plane in a CGI system. Here we compare experimentally measured computational ghost images reconstructed using speckle fields possessing either conventional or ND speckle. All of the images in Fig. 3 are reconstructed using the transverse intensity profile of the speckle calculated at the re-imaged aperture plane, which we denote as  $z=0$  (see Fig. 1(a)). Each column shows the reconstructed images when the object (shown as an inset at the bottom right) is axially displaced from the re-imaged aperture plane. The relative axial displacement of the object from the  $z=0$  is labelled at the top of each column.

The top row in Fig. 3 shows images recorded using conventional speckle generated from a disk in the Fourier plane of radius  $R = 2.3$  mm. The super-pixel configuration displayed on the SLM is shown on the left hand side in each case. At the  $z=0$  plane, the contrast of the image is high, but significant blurring is visible at depths greater than  $z=110$  mm. This blurring is caused by the decorrelation of the transverse intensity profile of the conventional speckle as it propagates, as discussed above. Of course, in order to bring the deeper images (top row, right hand side) back into focus, computational refocussing could be employed by recalculating the intensity cross-section of each projected speckle pattern at a deeper plane. The middle row shows images recorded using ND speckle generated from the same diameter limiting aperture as the top row. In this case the contrast is reduced at every plane (the point spread function of the system is discussed below). However, the transverse intensity profile of the ND speckle is

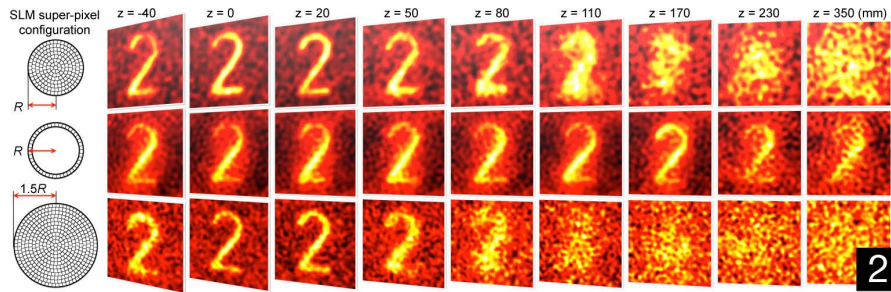


Fig. 3. Controlling the depth-of-field around a single plane in a CGI system. All images are reconstructed from 5500 speckle patterns. The transmissive object (1 mm in height) is shown as inset bottom right.  $R = 2.3$  mm. The super-pixels are of dimension  $\sim 0.3 \times 0.3$  mm in each case. Top row: images reconstructed using conventional speckle generated from a disk shaped aperture of radius  $r_{max} = R$  on the SLM. Middle row: images reconstructed using ND speckle generated from an annular shaped aperture of maximum radius  $r_{max} = R$  and minimum radius  $r_{min} = 2.0$  mm on the SLM. Bottom row: images reconstructed using conventional speckle generated from a disk shaped aperture of radius  $r_{max} = 1.5R$  on the SLM.

stable over a longer axial range, and so significant blurring only occurs at depths approaching  $z = 230$  mm, which gives a 2-3-fold enhancement in local DoF.

For equivalent aperture diameters, the average grain size of the ND speckle (middle row) is reduced by a factor of 1.5 in comparison with that of the conventional speckle (top row). The bottom row of Fig. 3 shows images recorded using conventional speckle with the same average grain size as the ND speckle. This is achieved by increasing the size of the disk on the SLM by a factor of 1.5, as shown on the left hand side of the bottom row. However, by increasing the diameter of the aperture, the local DoF of the CGI system is of course further reduced.

In this experiment it was convenient to generate ND speckle using an annular aperture displayed on an SLM. This allowed us to easily switch between ND and conventional speckle. However, as the central region of the SLM was blocked for the creation of ND speckle, this also reduced the amount of ‘useable’ light directed to the first order of the diffraction pattern to form the projected speckle field. For example, the total intensity of light in each ND speckle pattern used to reconstruct images shown in the middle row of Fig. 3 was  $\sim 24\%$  of that found in the conventional speckle using the whole aperture in the top row of Fig. 3. This situation could be rectified by placing an axicon before the SLM, so that light was focused to an annulus on the SLM, increasing the amount of light directed to the first order of the diffraction pattern [30, 31]. To compare the performance of the conventional and ND speckle imaging systems under constant illumination power, we kept the total intensity in the speckle patterns used in the middle and bottom rows approximately constant. The power was reduced in the experiments to reconstruct the bottom row of images by randomly selecting a subset of super-pixels from anywhere within a radius of  $1.5R$  for the generation of each speckle pattern, whose total area equalled that of the annular aperture. We found that this reduced the total intensity of the speckle patterns used in the bottom row of Fig. 3, but had no effect on the other imaging parameters of interest such as depth-of-field and point spread function.

### 3.2. Point spread function

We now describe the point spread function (PSF) of our CGI system in more detail. The PSF can be calculated from the autocorrelation of the intensity distribution of the speckle patterns, averaged over many realisations. The intensity autocorrelation can be derived from the autocorrelation of the underlying complex field [19]. Because of this, the PSF at the Fourier plane of the SLM is determined by the shape of the aperture on the SLM. Therefore in the case of conventional speckle, assuming that the SLM is illuminated with a plane wave, the PSF is defined by the square modulus of the Fourier transform of a circular aperture (of radius  $r$ ), i.e. the well-known Airy disk.

As shown in Fig. 4(a), the Airy disk PSF of the conventional speckle is circularly symmetric, with a radial intensity profile given by

$$I(\rho) = I_0 |J_1(k\rho r/f)/\rho|^2, \quad (4)$$

where  $\rho$  is the radial coordinate,  $I_0$  is a normalisation factor, and  $J_1$  is a Bessel function of the first kind, of order 1. The diameter of the central lobe of the Airy disk ( $D_C \approx 2.44\lambda f/D$ ) corresponds to the average speckle grain size of the conventional speckle. This also gives a measure of the minimum separation  $\delta S_{Cmin}$  at which two points may be independently resolved according to the Rayleigh criterion:  $\delta S_{Cmin} \approx (1/2)D_C$  in a diffraction limited system. The low intensity surrounding rings of the Airy disk indicate a small degree of lateral correlation between neighbouring speckle grains due to the hard edged nature of the aperture used to create them.

Equivalently, in the case of ND speckle, the PSF is given by the square modulus of the Fourier transform of an annulus, which may be calculated using Babinet's principle [18]. The PSF is also circularly symmetric with a profile along the radial coordinate  $\rho$  given by  $I_{ND}(\rho)$ :

$$I_{ND}(\rho) = I_0 \left| (r_{max}/\rho) J_1(k\rho r_{max}/f) - (r_{min}/\rho) J_1(k\rho r_{min}/f) \right|^2, \quad (5)$$

As  $r_{min} \rightarrow r_{max}$ ,  $I_{ND}(\rho) \rightarrow I_0 |J_0(k\rho r_{max}/f)|^2$  (where  $J_0$  is a Bessel function of the first kind, of order 0), which is the radial intensity profile of an idealised Bessel beam. Therefore, as  $r_{min} \rightarrow r_{max}$ ,  $D_{ND} \rightarrow \sim (2/3)D_C$ , and there is a corresponding 1.5-fold enhancement in the Rayleigh resolving power of the CGI system compared to that achievable using conventional speckle:  $\delta S_{ND} \rightarrow \sim (2/3)\delta S_C$ .

A plot of the PSF of our CGI system when using ND speckle is shown in Fig. 4(b), and it can be seen that the central lobe of Fig. 4(b) is narrower than that shown in Fig. 4(a). However the ND speckle PSF also inherits (from the Bessel-beam it is related to) the series of higher intensity rings surrounding the central lobe, which reduce the contrast of the resulting images. As the width of the annular aperture is reduced and the PSF approaches an idealised Bessel beam, the proportion of energy in these rings increases, more significantly reducing the contrast of the resultant images.

Figure 4(c-j) show a series of images of double slits of progressively reducing width and separation. The upper row shows images recorded using conventional speckle, and the lower row using ND speckle. These images were measured using the same parameters as Fig. 3 top and middle rows, with the same limiting aperture diameter in both cases. Figure 4(c-f) shows that the images measured using ND speckle suffer a reduction in contrast compared to images recorded using conventional speckle. However, as the separation between the slits is reduced (Fig. 4(g) and 4(h)), the enhanced Rayleigh resolving power of the ND speckle becomes evident. In Fig. 4(i) and 4(j), independent slits are only identifiable when using the ND speckle. The ringing of the Bessel-like PSF is also clearly visible in this case. Fig. 4(k) and 4(l) show simulations which also confirm this trade-off between Rayleigh resolving power and contrast.

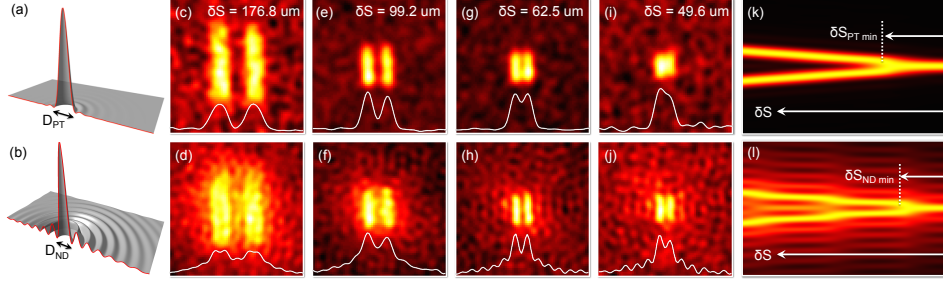


Fig. 4. CGI resolving power. Upper row (a,c,e,g,i,k) conventional speckle. Lower row (b,d,f,h,j,l) ND speckle. (a,b) PSFs. (b) shows  $I_{ND}(\rho)$  given by Eq. (5) with  $r_{min} = 0.87 r_{max}$  as in our experiments. (c-j) show a comparison of experimentally measured images of double slits in a modified 1951 USAF resolution test chart, imaged with conventional (upper row) and ND (lower row) speckle. The slit width and separation  $\delta S$  is given in each case. Cross-sections through the images of the slits are shown at the bottom of each image in white. The slits correspond to the following 1951 USAF resolution chart group-element labels: (c,d) 1-4, (e,f) 2-3, (g,h) 3-1, and (i,j) 3-2. (k,l) Simulation showing a comparison of the resolving power and contrast for conventional and ND speckle. Each vertical column of pixels in images (k) and (l) is a line-profile taken through two  $\delta$ -functions convolved with the conventional (k) and ND (l) PSFs. The height of the line profile is plotted as intensity. From right to left the separation between the  $\delta$ -functions,  $\delta S$ , is linearly increased. The separation at which the  $\delta$ -functions are no longer resolvable as separate points is marked as  $\delta S_{min}$ .

#### 4. Discussion

In this work we have investigated the performance of a CGI system using pseudo non-diffractive speckle patterns, which inherit their propagation characteristics from Bessel-beams. We note that previous studies have employed Bessel beams in a light-sheet microscope [26, 32] and in a point scanning imaging system [33], with emphasis on an investigation of the Bessel beam's apparent 'self-healing' properties. In this respect, we note that a Bessel beam *appears* to self-heal after an obstruction or after transport through a distorting medium, only if the rays forming the reconstructed beam further down-stream were themselves not significantly perturbed [34]. Therefore, as discussed in [32] any resistance to aberration will be highly dependent upon the nature and configuration of the scattering medium. In addition, the projection of ND speckle as demonstrated in our work is compatible with compressive sensing techniques to reduce the number of patterns required to form an image, which is not possible with a point scanning approach [14, 35].

In summary, we have demonstrated that using ND speckle in CGI permits a tuneable increase in the depth-of-field about a particular plane, and enhances the resolving power of the system by a factor of up to 1.5 for a given aperture diameter. The enhancement in resolving power is related to the phenomenon of optical super-oscillation, in which a globally band-limited signal can contain *local* regions that oscillate at a higher frequency than the global band-limit, at the expense of reduced contrast [36]. This is also true using ND speckle, as the highest spatial frequency recoverable across the entire field-of-view is still band limited, while local regions of higher spatial frequency can be recovered as we have demonstrated. ND speckle has also previously been shown to exhibit a greater super-oscillatory area fraction than conventional speckle [37, 38]. As low spatial frequencies are cut out of the ND speckle patterns, there is also an accompanying reduction in image contrast, and slowly varying information is lost. Deconvolution guided by any additional a priori knowledge of the scene being imaged could be

applied to partially correct for this loss in contrast [21]. We note that digital deconvolution also has the advantage that it can be designed to perform non-linear processes, while Fourier optics is limited to linear optical information processing.

Of course, the modification of the imaging parameters in our CGI system is analogous to the effect of inserting an annular spatial filter into the Fourier plane of a conventional detector array based imaging system. However, the Bessel-like PSF found in our images only emerges after an ensemble of patterns have been projected. This highlights the link between correlations in projected intensity patterns and the resulting PSF of a CGI system, which may facilitate the design of a range of novel PSFs in the future [39].

### **Acknowledgements**

We acknowledge financial support from the U.K. Engineering and Physical Sciences Research Council (EPSRC) (QuantIC, Grant no. EP/M01326X/1), and the European Research Council (ERC) (TWISTS, Grant no. 192382). D.B.P thanks the Royal Academy of Engineering for support. R.Q.H acknowledges support from the National Natural Science Foundation of China (Grant no. 61501242) and the Chinese Scholarship Council (Grant no. 201406840020). D.B.P would like to thank Miguel Angel Olvera Santamaria, Mark Dennis and Johannes Courtial for useful discussions, and Gabriel Spalding for critical reading of the manuscript.